# High-Resolution Short-Circuit Fault Localization in a Multilayer Integrated Circuit Using a Quantum Diamond Microscope

P. Kehayias,[1,*] J. Walraven,[1] A.L. Rodarte,[1] and A.M. Mounce[2]

[1] *Sandia National Laboratories, Albuquerque, New Mexico 87185, USA*

[2] *Center for Integrated Nanotechnologies, Sandia National Laboratories, Albuquerque, New Mexico 87123, USA*

(Received 27 February 2023; revised 8 May 2023; accepted 26 June 2023; published 18 July 2023)

As integrated-circuit (IC) geometry and packaging become more sophisticated with ongoing fabrication and design innovations, the electrical-engineering community needs increasingly powerful failure-analysis (FA) methods to meet the growing troubleshooting challenges of multilayer (with multiple metal layers) and multichip components. In this work, we investigate an electronics FA method using a quantum diamond microscope (QDM) to image the magnetic fields from short-circuit faults. After quantifying the performance by detecting short-circuit faults in a multilayer silicon die, we assess how a QDM would detect faults in a heterogeneously integrated (HI) die stack. This work hopefully establishes QDM-based magnetic imaging as a competitive technique for electronics FA, offering high spatial resolution, high sensitivity, and robust instrumentation. We anticipate these advantages to be especially useful for finding faults deep within chip-stack ICs with many metal layers, optically opaque layers, or optically scattering layers.

DOI: 10.1103/PhysRevApplied.20.014036

## I. INTRODUCTION

Integrated-circuit (IC) feature sizes continue to shrink in accordance with Moore's law, and it is important for electronics failure-analysis (FA) techniques to keep up with new process technologies [1,2]. FA techniques must be able to identify defects in devices with denser layouts, weaker signals, and multiple stacked dice [3,4]. The shrinking geometries of planar transistors (down to 26 nm), fin field-effect transistors (FinFETs) (down to 5 nm), and gate-all-around (GAA) transistors (down to 3 nm) and the increasing complexity of "more than Moore" devices all pose new FA difficulties [5]. Furthermore, many existing FA methods struggle to find faults in the bottom layers of components made from multiple stacked dice. Having accurate information of the number of faults in a device and their locations in two or three dimensions (including depth) helps identify the root cause of the IC production problem. This motivates a constant pursuit of new FA approaches to keep up with the increasing challenge, with the goal of being able to locate weak faults (with small signal amplitudes) deep inside a device with high spatial resolution and quick measurement time.

In this paper, we consider several leading electronics FA techniques, including scanning-optical-microscope approaches, thermal-based approaches, and magnetic imaging approaches [1,2]. With magnetic imaging, we measure the magnetic fields emitted from the internal electric currents, then use the magnetic field maps to locate short-circuit faults. Magnetic imaging is appealing because most IC materials (insulators, doped semiconductors, and metals) are transparent to magnetic fields, making it possible to look deep into an otherwise opaque device. In addition, high-performance magnetometers can sense weak magnetic fields, allowing us to detect and localize weak currents quickly.

When choosing a magnetic imaging technology for electronics FA, it is important to consider the magnetic sensitivity (noise floor), the signal-to-noise ratio (SNR), the spatial resolution, and the measurement stand-off distance between the sensor and the magnetic sources. The SNR and the spatial resolution are closely related to the stand-off distance; increasing the stand-off distance generally leads to weaker magnetic fields and a coarser spatial resolution [6]. This suggests that an ideal magnetic imager should minimize the stand-off distance to achieve the best SNR and spatial resolution. In addition, it is important to consider the technical details of the apparatus, including its operating conditions (e.g., temperature), frequency range, and uptime. A standard tool for magnetic imaging is a scanning superconducting quantum interference device (SQUID) microscope [7]. Despite being a mature commercially available instrument with a good magnetic noise floor, one weakness is that it scans a cryogenic sensor head across a room-temperature device, leading to a

*pmkehay@sandia.gov

 

coarse spatial resolution (approximately 50–100 μm) and low uptime.

Quantum magnetic sensing using nitrogen-vacancy (N-$V$) centers in diamond is an emergent technique that enables high spatial resolution, high magnetic sensitivity, and integration with a variety of targets. One realization of this technology is the quantum diamond microscope (QDM) [8–10], which circumvents the above drawbacks and is the focus of this work. By placing a synthetic diamond sample with a thin surface layer of magnetically sensitive N-$V$ centers directly on top of a device, illuminating the N-$V$ layer with laser light, and imaging the N-$V$ fluorescence with a wide-field optical microscope, we measure the magnetic field in each pixel using a camera. The QDM advantages include a stand-off distance that can be made very small (approximately 2-μm air gap [11]), a micron-scale spatial resolution, operation in ambient conditions, and nearly 100% up time. Earlier works have shown how a QDM can image the magnetic fields from commercial ICs and other semiconductor devices [12–15]. Given that QDMs already perform well when measuring working electronic devices and the advantages listed above, this makes them promising for locating short-circuit faults in broken devices.

In this work, we use a QDM apparatus to locate short-circuit faults between two conducting layers in an application-specific integrated circuit (ASIC). We present six faults found in two dice, which are caused by copper defects between two conducting layers. To benchmark our technique against an established (thermal) FA method, we also use a thermally induced voltage alteration (TIVA) imaging instrument to locate faults in the same two dice [16,17]. TIVA is a standard electronics FA tool that uses laser heating to locate faults. While N-$V$ magnetic imaging and TIVA imaging differ in their technical maturity, operating principles, and limitations, both techniques detect short-circuit faults in the same locations, confirming that a QDM can perform FA. Furthermore, we find that our QDM apparatus is able to detect faults with a 35 times better SNR than the TIVA instrument, meaning that a QDM can find weaker faults considerably faster (1200 times faster for the same SNR). Our QDM instrument locates two faults that are not seen with TIVA imaging, confirming the QDM SNR advantage. This work hopefully establishes the QDM as a high-performance apparatus for short-circuit fault localization and we conclude with additional insights on how a QDM FA tool should work with heterogeneously integrated (HI) devices.

## II. RESULTS

### A. Device under test

Our device under test (DUT) is a silicon ASIC die (see the Supplemental Material [18]). It is $27.45 \times 26.05$ mm$^2$ in size and the outer perimeter is lined with pads. This DUT contains no magnetic materials contributing background fields (e.g., solder bumps [19,20]), meaning that any detected magnetic fields are due to the applied current. Internally, the DUT has multiple conducting layers and is known from initial testing to have short-circuit faults between the power planes in layers 4 and 5 [(2–10)-Ω resistance between the relevant pads]. However, the number of faults and their locations are not known *a priori*. Our tasks are to test whether we can locate the short-circuit faults with a QDM setup, compare with the fault locations located with a TIVA-imaging setup, and compare the performance between the two instruments.

Figure 1 shows optical images of the lower-left and lower-right corners of the DUT, where we search for short-circuit faults. We present the results for two such dice. The fields of view being imaged are indicated as FOV1 and FOV2 for die 1 and die 2, respectively. We apply a test current between two pads using probe tips, then use N-$V$ magnetic imaging and TIVA imaging to search for short-circuit faults.

For the N-$V$ magnetic imaging experiments, we use a custom-made QDM apparatus with built-in probe-tip manipulators to apply current to the relevant pads. The magnetic field images show the measured magnetic field component along the diamond [111] crystallographic direction ($B_{111}$), which is approximately 35° out of plane. For the TIVA measurements, we use a commercial system with a 1342-nm probe laser. Full details and schematics of the setups are included in the Supplementary Material [18].

### B. QDM imaging and TIVA imaging for FOV1

Figure 2 shows two overlaid N-$V$ magnetic images and a TIVA image near the lower-right corner of a die (FOV1). We apply a 50-mA test current for the N-$V$ magnetic imaging experiments and a 100-mA test current for the TIVA imaging experiment. As the applied current disperses from the input pad and converges toward the output pad, it creates a grid pattern in the magnetic images similar to the grid pattern of layers 4 and 5. The grid pattern contains defects caused by current traveling between layers 4 and 5 along the $z$ axis, indicating short-circuit faults (labeled A, B, and C). For comparison, the faults in the TIVA images appear as circular features (where laser heating at the fault location modifies the resistance) on top of a nominally uniform background.

These initial results confirm that N-$V$ magnetic imaging can locate the same faults as TIVA imaging, a well-established FA technique. This is especially promising because the two methods use different phenomena to detect faults; N-$V$ magnetic imaging senses the internal currents in a device (both the intended and unintended current paths), while TIVA imaging detects changes in the DUT power demand caused by the increased resistance from laser heating of metal defects in the current path, which

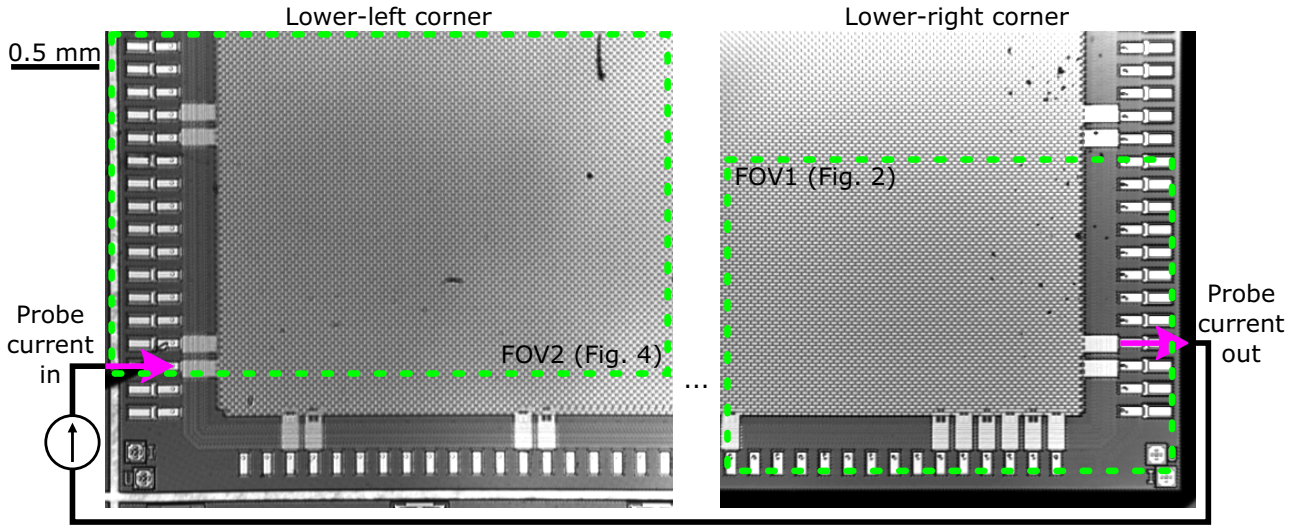


FIG. 1. Photographs of the lower-left and lower-right corners of the DUT that we investigate in this work. We apply a probe current to a pad near the lower-left corner, after which it flows through the DUT and is collected from a pad near the lower-right corner. The green boxes indicate the fields of view (FOVs) shown in later figures.

may be responsible for short-circuit faults. To benchmark how N-$V$ magnetic imaging performs compared to TIVA imaging for this device, we now compare the SNR and the spatial resolution of each technique for fault B.

### C. SNR assessment

The QDM SNR is given by

$$\mathrm{SNR}_{\mathrm{QDM}} = \frac{B_{\mathrm{fault}}}{\delta B}.$$

Here, $B_{\mathrm{fault}}$ is the magnetic field amplitude associated with a fault (normalized to a 1-A test current) and $\delta B$ is the standard deviation of the measured magnetic fields normalized to a 1-s measurement duration and a $1 \times 1\ \mu\mathrm{m}^2$ pixel size. $\delta B$ is set by the photon shot noise of the N-$V$ fluorescence collected by the camera; it improves linearly with the pixel area and improves proportional to the square root of the measurement duration. We find that $\delta B = 30\ \mu\mathrm{T}$. Although $\delta B$ is up to 4–8 times better in our earlier works [13], here we reduce the laser power to minimize the risk of damaging the DUT or altering its internal currents due to stray light. Finally, if the current in the DUT is traveling through a resistive network, then $B_{\mathrm{fault}}$ is proportional to the test current.

In Figs. 3(a) and 3(b), we evaluate $B_{\mathrm{fault}}$ for fault B. This is nontrivial to evaluate because we have to separate the $B_{\mathrm{fault}}$ amplitude from the grid pattern superimposed on the fault and both have comparable amplitudes. To separate them, we take the Fourier transform of Fig. 3(a) and set the amplitudes of the frequency components from the grid pattern to zero. After calculating the inverse Fourier transform (with a suppressed grid pattern), we remove a quadratic background magnetic field. These fault-isolation steps yield the magnetic field map of the isolated fault in Fig. 3(b). Fault B has a 7.7-$\mu$T amplitude when using a 50-mA test current, which leads to $\mathrm{SNR}_{\mathrm{QDM}} = 5.1$ for a 1-A test current, 1-s measurement duration, and $1 \times 1\ \mu\mathrm{m}^2$ pixel size.

Similarly, the TIVA-imaging SNR is given by

$$\mathrm{SNR}_{\mathrm{TIVA}} = \frac{V_{\mathrm{fault}}}{\delta V}.$$

Here, $V_{\mathrm{fault}}$ is the TIVA voltage associated with a fault (normalized to a 1-A test current) and $\delta V$ is the standard deviation of the measured voltages in the FOV normalized to a 1-s measurement duration and a $1 \times 1\ \mu\mathrm{m}^2$ pixel size. Here, we assume uncorrelated white noise, meaning that $\delta V$ improves linearly with the pixel area and improves proportional to the square root of the measurement duration. Furthermore, since TIVA imaging is a raster-scanning measurement, $\delta V$ scales with the square root of the image area for a given pixel size. We normalize the TIVA scan area to the QDM image area ($1.31\ \mathrm{mm} \times 2.09\ \mathrm{mm} = 2.74\ \mathrm{mm}^2$). Finally, $V_{\mathrm{fault}}$ should likely scale with current. If the total resistance of the DUT ($R_0$) is proportional to that of a low-resistance fault between layers 4 and 5, then laser heating should modify the resistance to $R_0 + \Delta R$, where $\Delta R = R_0 \alpha \Delta T$, $\alpha$ is a temperature coefficient, and $\Delta T$ is the temperature change. Under constant-current operation, $V_{\mathrm{fault}} = \Delta V = I \Delta R$, so $V_{\mathrm{fault}}$ should be proportional to the applied current and the probe laser power.

The TIVA SNR depends on many additional factors, including the laser scan rate, averaging procedure, current-supply response and bandwidth, and voltage-amplifier response and bandwidth. The noise floor is usually set by

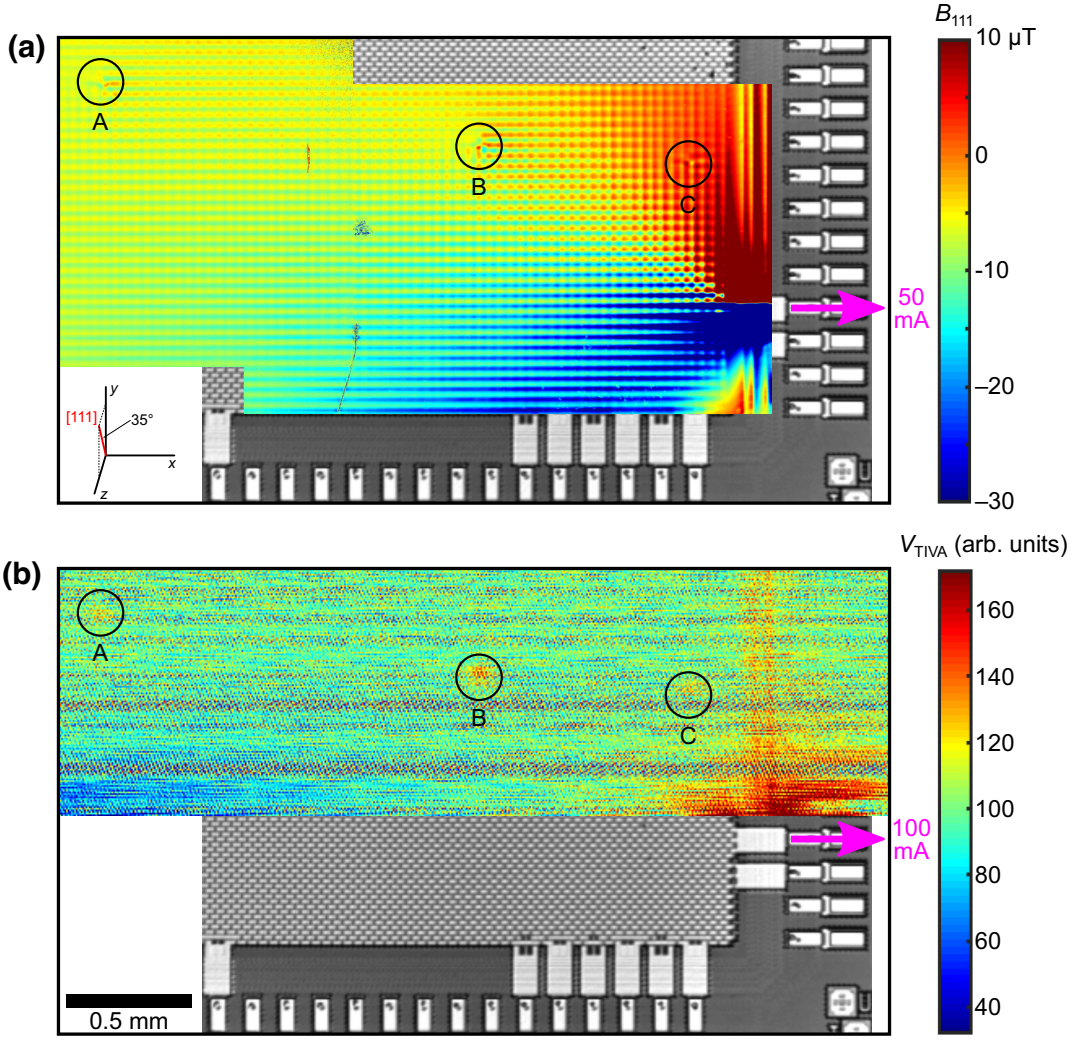


FIG. 2. (a) N-$V$ magnetic images with a 50-mA test current, with faults A–C circled. The extra scratch marks are due to defects in the diamond surface. (b) A TIVA image with a 100-mA test current, showing faults A–C in the same locations.

the current-supply noise and the voltage-amplifier noise, which also determine the background amplitude [$V_{bg} = 96$ in Figs. 3(c) and 3(d)]. Since the TIVA SNR is highly sample dependent, we tune the above parameters to optimize the TIVA sensitivity and maximize the SNR.

In Figs. 3(c) and 3(d), we evaluate $V_{fault}$ and $\delta V$ for fault B. We fit the fault image with a two-dimensional (2D) Gaussian function to find $V_{fault} = 32$ and $\delta V = 19$ in arbitrary units. Applying the relevant normalization factors, we obtain $SNR_{TIVA} = 0.15$ for a 1-A test current, a 1-s measurement duration, a $1 \times 1\ \mu m^2$ pixel size, and a 2.74 $mm^2$ image area.

Comparing $SNR_{QDM} = 5.1$ and $SNR_{TIVA} = 0.15$, we find that $SNR_{QDM}$ is 35 times larger for fault B. This indicates a substantial sensitivity advantage when using N-$V$ magnetic imaging, allowing us to find weaker faults in less measurement time. Note that this SNR comparison may not be generalizable to all faults in the DUT. Although both techniques are sensitive to the current in the defect, $SNR_{TIVA}$ depends on other factors that do not affect $SNR_{QDM}$, such as how much nearby metal is contributing to the heat sinking. Despite this detail, our SNR assessment gives us confidence that N-$V$ magnetic imaging can locate weaker faults than TIVA imaging. To confirm this finding, we study a second die (FOV2 in Fig. 1) with weaker faults that are detectable with N-$V$ magnetic imaging but not with TIVA imaging in normal operating conditions, as described below.

### D. Spatial-resolution comparison

Spatial resolution has a variety of definitions, including the point-spread-function line width, the optical diffraction limit, or the closest distance before two features become indistinguishable. For this analysis, we define spatial resolution as fault-localization uncertainty, or how tightly we

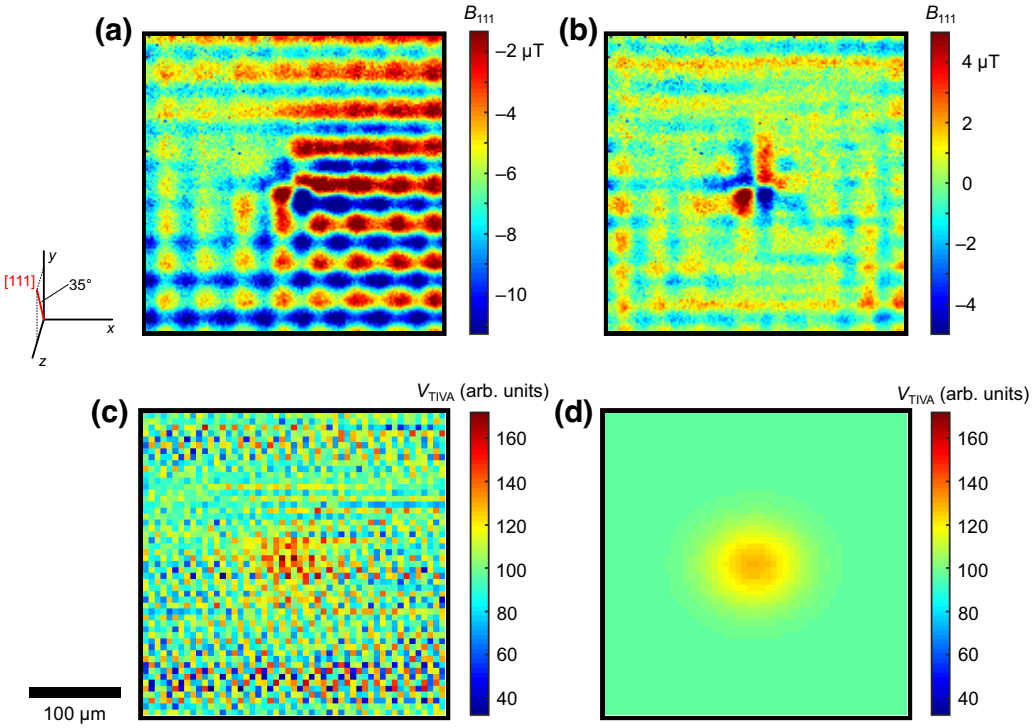


FIG. 3. (a) A QDM magnetic image for fault B. (b) A magnetic image after suppressing the background magnetic fields, removing the grid pattern in the Fourier transform, and removing a quadratic background field. From this image, we extract a $B_{\text{fault}} \approx 7.7$ μT fault amplitude when applying a 50-mA test current. (c) A TIVA image for fault B. (d) The two-dimensional (2D) Gaussian fit for the TIVA image, from which we extract $V_{\text{fault}} = 32$ and $\delta V = 19$ for the fault amplitude and noise floor when applying a 100-mA test current. Note that both methods have a 20-min experiment duration but the TIVA imaging experiment has a 2-times-larger test current, approximately (3 × 3)-times-larger pixels, and an almost 4-times-larger area.

can localize an isolated fault in the $x$-$y$ plane, which is the spatial-resolution metric relevant to electronics FA.

For N-$V$ magnetic imaging, fault B has a location uncertainty of about 0.7 μm, calculated from the cross shape in Fig. 3(b) and the $\delta B$ noise floor (see the Supplemental Material [18]). The lobes in Fig. 3(b) have approximately 20-μm spacing and width, which suggests that neighboring faults could be as close as approximately 20 μm before they begin to blend together. Note that the $x$-$y$ location of a fault within the 8 μm × 8 μm overlap between the traces in layers 4 and 5 causes very different magnetic images. Simulating this phenomenon and comparing to the experimental magnetic images can yield a fault-position uncertainty significantly smaller than the 16-μm periodicity for these conducting layers. For the TIVA image, the 2D Gaussian fit in Fig. 3(d) has a standard deviation of 34 μm. This standard deviation provides an estimate for the spatial resolution, although the centroid uncertainty can be made arbitrarily small with a sufficiently good SNR. Overall, we conclude that our QDM spatial resolution is $\gtrsim 10$ times better than the TIVA-imaging spatial resolution, although both could be enhanced with additional hardware improvements and postprocessing efforts.

The spatial resolution for both techniques is limited by the optical-diffraction limit $d = \lambda/2\text{NA}$, where λ is the fluorescence (illumination) wavelength for the QDM (TIVA) instrument and NA is the microscope-objective numerical aperture. We obtain $d_{\text{QDM}} = 1.4$ μm for our QDM apparatus ($\lambda = 700$ nm, NA = 0.25) and $d_{\text{TIVA}} = 4.8$ μm for our TIVA apparatus ($\lambda = 1342$ nm, NA = 0.14). Given the same NA, $d_{\text{QDM}}$ should be 1.9 times better than $d_{\text{TIVA}}$. Both could be improved with a better NA, although N-$V$ magnetic imaging can also employ superresolution microscopy or atomic force microscopy (AFM) techniques [21,22]. In practice, the stand-off distance usually limits the QDM spatial resolution, while heat spreading usually limits the TIVA spatial resolution [23,24].

### E. QDM imaging and TIVA imaging for FOV2

Figure 4 shows magnetic and TIVA images for a second die, in an area closer to the middle of the die where the currents are weaker. We apply a 100-mA test current for both the N-$V$ magnetic imaging and the TIVA-imaging experiments and we see three additional short-circuit faults,

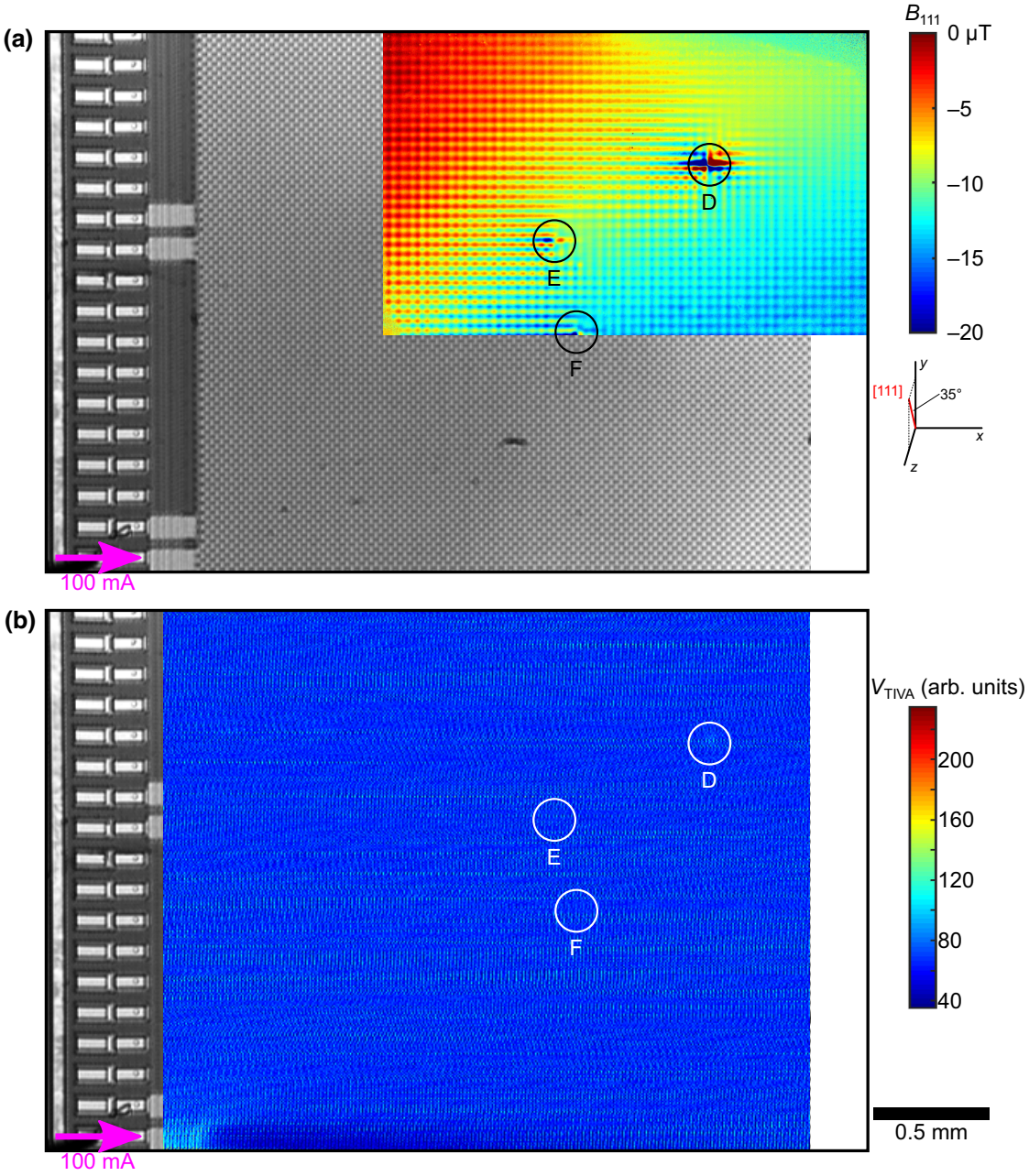


FIG. 4. (a) The QDM magnetic image for FOV2, showing faults D–F. (b) The TIVA image for FOV2, showing the same three fault locations. Fault D is visible, but faults E and F are too weak to see.

labeled D, E, and F. Both techniques see a strong short-circuit fault (fault D), although it is barely visible in the TIVA image. Furthermore, the N-$V$ magnetic image reveals two additional faults (faults E and F), which have magnetic field amplitudes that are approximately 20–40 times weaker than that of fault D. Faults E and F are too weak to see in the TIVA image, confirming our earlier finding that $SNR_{QDM}$ is better than $SNR_{TIVA}$. Given knowledge of their locations from the magnetic image, we are later able to locate them after several SNR enhancements to the TIVA measurement (see the Supplemental Material [18]).

After finishing the QDM- and TIVA-imaging experiments, we use a focused ion beam (FIB) to cross section the DUT at the fault locations, then use a scanning electron microscope (SEM) to image the cross sections. Figure 5 includes a cross section for fault F, showing the copper defect that causes a short between the conducting layers.

## III. MAGNETIC IMAGING FOR AN HI DEVICE

Having established N-$V$ magnetic imaging as a promising electronics FA approach for locating short-circuit

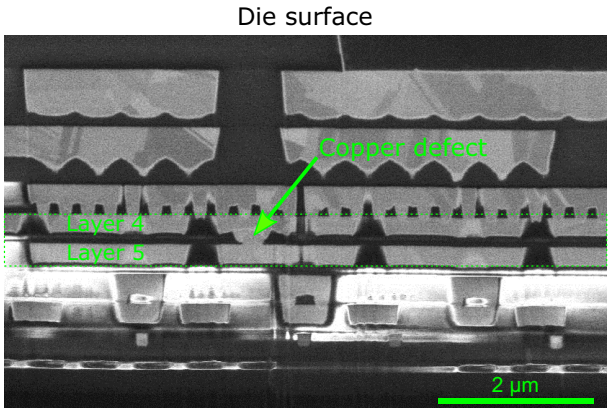


FIG. 5. A scanning-electron-microscope (SEM) image of a die cross section showing fault F, which is caused by a copper defect between layers 4 and 5.

faults, we now consider how this approach can be used for a broader range of devices. Perhaps the most challenging devices for N-$V$ magnetic imaging to measure are those with weak currents in deep layers (i.e., ICs with many conducting layers and stacked dice), since the magnetic field amplitude and spatial resolution will degrade with the increased stand-off distance.

The DUTs imaged in Figs. 2 and 4 are intended to be part of an HI device, with an additional 30-μm die to be mounted on top. To simulate the magnetic images for short-circuit faults if they are measured in an HI device, we calculate the expected magnetic field images with 30 μm of additional stand-off distance [6], shown in Fig. 6. We evaluate the anticipated performance for three typical fault magnetic amplitudes: strong (fault D), medium (fault E), and weak (fault A). As expected, the grid patterns and fault features become weaker and coarser, but fortunately the fault features are still visible with the added stand-off distance, especially after using the fault-isolation steps described above. This suggests that N-$V$ magnetic microscopy could also work well for HI devices, despite the increased stand-off distance. However, since weak magnetic features become more difficult to isolate from the background magnetic field with increasing stand-off distance, minimizing the measurement stand-off distance is always preferable. Despite these limitations, fault D (which has a large $B_{\text{fault}} \approx 120$ μT amplitude and a small background gradient) should be visible as far away as approximately 150 μm. This suggests that

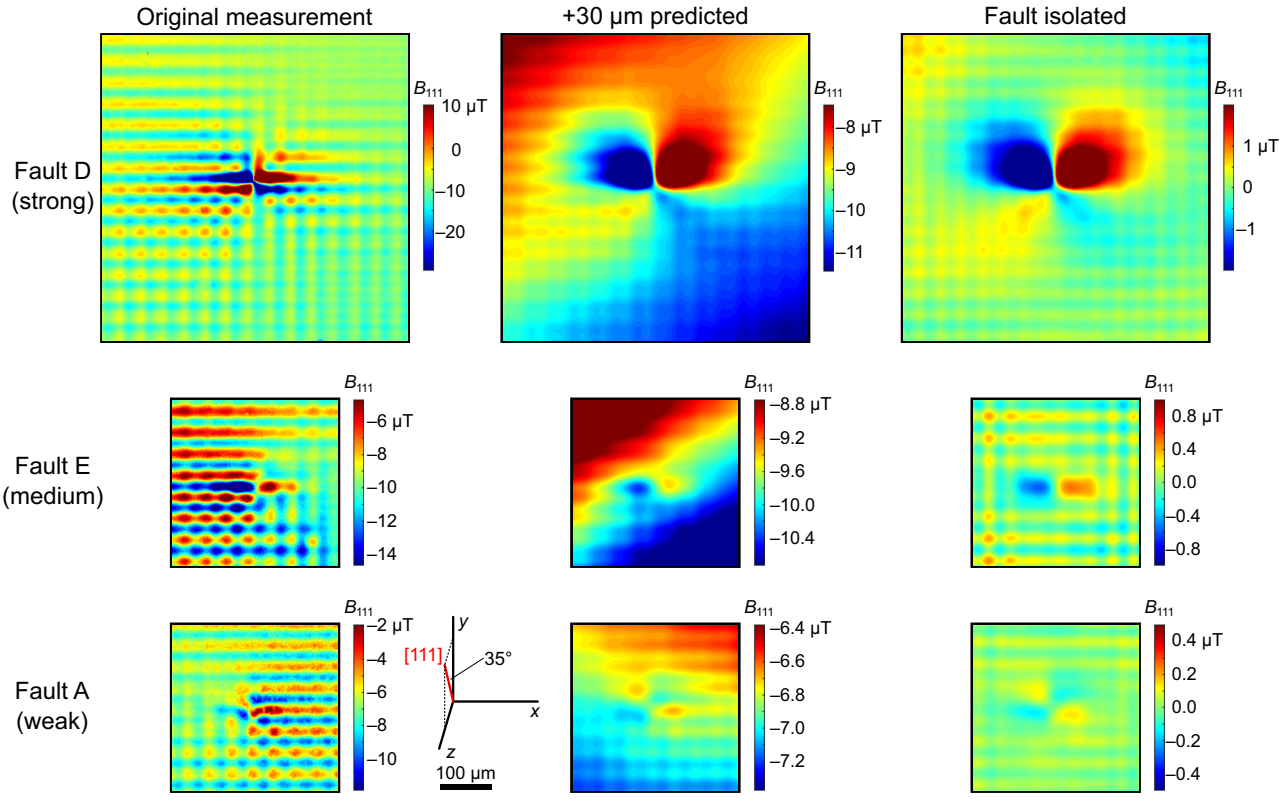


FIG. 6. Magnetic images for faults D, E, and A, representing strong-, medium-, and weak-amplitude faults. Using the measured magnetic images (left column), we simulate the magnetic images if the die is part of an HI device, with an additional 30-μm die on top (middle column). We apply the same fault-isolation postprocessing to remove the background ripples and gradients as in Fig. 3 (right column).

magnetic imaging (using a QDM or other methods) could still be viable for finding short-circuit faults deep within HI devices, stacked-die ICs, devices using backside power delivery, and other devices with limited optical access to the deep layers.

## IV. DISCUSSION

Magnetic imaging and TIVA imaging have different strengths and trade-offs when used to locate short-circuit faults. With magnetic imaging, the magnetic field amplitude and spatial resolution get worse with larger stand-off distance, but the magnetic signal should be unimpeded by any materials (metals, semiconductors, or insulators) between the fault and the sensor. For TIVA imaging, the materials matter; it is difficult to find a fault surrounded by metal due to its opacity and thermal conductivity. However, transparent semiconductor and insulator layers should not impede the performance significantly (e.g., imaging conducting layers through back of the bulk-silicon substrate). Despite its reduced sensitivity to deeper sources, magnetic imaging can still be an appealing choice for finding faults in multilayer dice, stacked-die devices, and HI devices. In particular, if a fault is in a lower die under dense metallization with high interconnect density and underfill, magnetic imaging could be a viable FA option despite the performance sacrifice, while TIVA imaging might be impossible.

Compared to other magnetic imaging approaches, such as scanning SQUID microscopy, scanning giant magnetoresistance (GMR) microscopy, scanning magnetic tunnel junction (MTJ) microscopy, and magnetic force microscopy (MFM), N-$V$ magnetic imaging offers several advantages [25–28]. Unlike these other techniques, a QDM acquires the magnetic information in all pixels simultaneously (rather than raster scanning). This means that a QDM has no moving parts when running, which is ideal when testing devices energized using probe tips. This also means that any drift during acquisition should be common to all pixels and easily removed, while drift during a raster-scanning experiment may be difficult to remove. Finally, a QDM can operate in ambient conditions, does not require a magnetic shield, has nearly 100% up time, and is inexpensive compared to other FA tools. These features make a QDM approach appealing to the electronics FA, power electronics, microelectronics manufacturing, very large-scale integration (VLSI), and multichip-module (MCM) communities.

Since the N-$V$ stand-off distance can be as small as a few microns, this suggests that single-die applications and applications allowing device thinning are ideal for QDM FA, although this is generally true for most FA techniques. We note that these applications are where a QDM instrument excels and that the expected performance sacrifice for deep faults does not prevent a QDM from still being useful. For short-circuit faults deeper than approximately 100 $\mu$m, a scanning SQUID microscope will likely outperform a QDM for fault detection, although the QDM suitability for 2D, 2.5D, and 3D-dimensional, and three-dimensional components depends on the overall device thickness. This is because for deep faults, we are unable to exploit the QDM advantage of having a few-micron stand-off distance (the N-$V$ and SQUID stand-off distances will be comparable) and a scanning SQUID microscope should have a better magnetic noise floor (approximately 20 $\mathrm{pT}/\sqrt{\mathrm{Hz}}$) [29]. However, a scanning SQUID microscope measuring the $B_z$ component of the magnetic field is insensitive to currents in the $z$ direction. The vector magnetic field information from a QDM could be used to extract more insights about the devices being measured but this comes at the cost of worse magnetic sensitivity and additional N-$V$ orientations to measure (leading to a slower measurement). From this work (and previous examples using scanning SQUID microscopes), we find that single-axis magnetic measurements work well for magnetic anomaly detection for electronics FA, while the further advantages of vector imaging are under investigation. Finally, any image-analysis techniques used to enhance the spatial resolution of a coarse-resolution magnetic imager can also be applied to QDM images, with the added benefit of the preprocessed magnetic image having a closer stand-off distance.

## V. CONCLUSIONS

In this work, we investigate how an N-$V$ magnetic imaging apparatus can be used for electronics FA by locating short-circuit faults between conducting power planes in a multilayer silicon ASIC device. Validating N-$V$ magnetic imaging with the industry-standard TIVA imaging technique, we find that N-$V$ magnetic imaging has a significantly better SNR (35 times better for fault B) and spatial resolution, meaning that we can find weaker faults (e.g., faults E and F) in less time (1200 times faster for the same SNR) with tighter location uncertainty. We also show that QDM imaging can be extended to HI devices and ICs made with stacked dice. As a result, we hope that this work establishes the QDM as an effective instrument for short-circuit fault localization. We anticipate further exploration into how QDM vector magnetic imaging, sophisticated forward-model and inverse-model calculations, or magnetic image analysis using a machine-learning algorithm may benefit fault localization [19,20,30]. In addition, the use of a QDM apparatus to image AC magnetic fields could open up new electronics FA possibilities as well [31]. Finally, similar performance comparisons to other FA technologies (e.g., lock-in thermography, or LIT [32]) will further identify the unique role that N-$V$ magnetic imaging can play in solving FA problems.

## ACKNOWLEDGMENTS

We thank Paiboon Tangyunyong and Edward Cole for their technical advice on the manuscript and William Mook for his work in producing the FIB cross-section images. Sandia National Laboratories is a multimission laboratory managed and operated by National Technology and Engineering Solutions of Sandia, LLC, a wholly owned subsidiary of Honeywell International, Inc., for the U.S. Department of Energy (DOE) National Nuclear Security Administration under Contract DE-NA0003525. This work was funded, in part, by the Laboratory Directed Research and Development Program and performed, in part, at the Center for Integrated Nanotechnologies, an Office of Science User Facility operated for the DOE Office of Science.

[1] T. Gandhi, *Microelectronics Failure Analysis: Desk Reference* (ASM International, Materials Park, Ohio, USA, 2019).

[2] L. C. Wagner, *Failure Analysis of Integrated Circuits: Tools and Techniques* (Springer, New York, USA, 1999), Vol. 494.

[3] R. Chau, in *2019 IEEE International Electron Devices Meeting (IEDM)* (2019), p. 1.1.1, https://ieeexplore.ieee.org/document/8993462.

[4] E. P. DeBenedictis, M. Badaroglu, A. Chen, T. M. Conte, and P. Gargini, Sustaining Moore's law with 3D chips, Computer **50**, 69 (2017).

[5] M. Graef, in *2021 IEEE International Roadmap for Devices and Systems Outbriefs* (2021), p. 1, https://ieeexplore.ieee.org/document/9827536.

[6] E. A. Lima and B. P. Weiss, Obtaining vector magnetic field maps from single-component measurements of geological samples, J. Geophys. Res.: Solid Earth **114**, B06102 (2009).

[7] C. L. Henderson, Failure analysis techniques for a 3D world, Microelectron. Reliab. **53**, 1171 (2013).

[8] D. R. Glenn, R. R. Fu, P. Kehayias, D. Le Sage, E. A. Lima, B. P. Weiss, and R. L. Walsworth, Micrometer-scale magnetic imaging of geological samples using a quantum diamond microscope, Geochem. Geophys. Geosyst. **18**, 3254 (2017).

[9] E. V. Levine, M. J. Turner, P. Kehayias, C. A. Hart, N. Langellier, R. Trubko, D. R. Glenn, R. R. Fu, and R. L. Walsworth, Principles and techniques of the quantum diamond microscope, Nanophotonics **8**, 1945 (2019).

[10] S. C. Scholten, A. J. Healey, I. O. Robertson, G. J. Abrahams, D. A. Broadway, and J.-P. Tetienne, Widefield quantum microscopy with nitrogen-vacancy centers in diamond: Strengths, limitations, and prospects, J. Appl. Phys. **130**, 150902 (2021).

[11] P. Kehayias, E. Bussmann, T.-M. Lu, and A. M. Mounce, A physically unclonable function using NV diamond magnetometry and micromagnet arrays, J. Appl. Phys. **127**, 203904 (2020).

[12] M. J. Turner, N. Langellier, R. Bainbridge, D. Walters, S. Meesala, T. M. Babinec, P. Kehayias, A. Yacoby, E. Hu, M. Lončar, R. L. Walsworth, and E. V. Levine, Magnetic Field 555 of Integrated-Circuit Activity with a Quantum Diamond Microscope, Phys. Rev. Appl. **14**, 014097 (2020).

[13] P. Kehayias, E. V. Levine, L. Basso, J. Henshaw, M. Saleh Ziabari, M. Titze, R. Haltli, J. Okoro, D. R. Tibbetts, D. M. Udoni, E. Bielejec, M. P. Lilly, T.-M. Lu, P. D. D. Schwindt, and A. M. Mounce, Measurement and Simulation of the Magnetic Fields from a 555 Timer Integrated Circuit Using a Quantum Diamond Microscope and Finite-Element Analysis, Phys. Rev. Appl. **17**, 014021 (2022).

[14] L. Basso, P. Kehayias, J. Henshaw, M. Saleh Ziabari, H. Byeon, M. P. Lilly, E. Bussmann, D. M. Campbell, S. Misra, and A. M. Mounce, Electric current paths in a Si:P delta-doped device imaged by nitrogen-vacancy diamond magnetic microscopy, Nanotechnology **34**, 015001 (2022).

[15] S. Scholten, G. Abrahams, B. Johnson, A. Healey, I. Robertson, D. Simpson, A. Stacey, S. Onoda, T. Ohshima, T. Kho, J. Ibarra Michel, J. Bullock, L. Hollenberg, and J.-P. Tetienne, Imaging Current Paths in Silicon Photovoltaic Devices with a Quantum Diamond Microscope, Phys. Rev. Appl. **18**, 014041 (2022).

[16] E. J. Cole, P. Tangyunyong, and D. Barton, in *IEEE International Reliability Physics Symposium Proceedings* (1998), p. 129, https://ieeexplore.ieee.org/document/670462.

[17] E. Cole, P. Tangyunyong, D. Benson, and D. Barton, TIVA and SEI developments for enhanced front and backside interconnection failure analysis, Microelectron. Reliab. **39**, 991 (1999).

[18] See the Supplemental Material at http://link.aps.org/supplemental/10.1103/PhysRevApplied.20.014036 for further details on the device under test, experimental setups, and image analysis.

[19] E. V. Levine, M. J. Turner, N. Langellier, T. M. Babinec, M. Loncar, and R. L. Walsworth, in *International Symposium for Testing and Failure Analysis* (2020), p. 84, https://dl.asminternational.org/istfa/proceedings-abstract/ISTFA2020/83348/84/15399.

[20] S. M. Oliver, D. J. Martynowych, M. J. Turner, D. A. Hopper, R. L. Walsworth, and E. V. Levine, in *International Symposium for Testing and Failure Analysis* (2021), p. 96, https://dl.asminternational.org/istfa/ISTFA2021/volume/84215.

[21] X. Chen, C. Zou, Z. Gong, C. Dong, G. Guo, and F. Sun, Subdiffraction optical manipulation of the charge state of nitrogen vacancy center in diamond, Light: Sci. Appl. **4**, e230 (2015).

[22] P. Maletinsky, S. Hong, M. S. Grinolds, B. Hausmann, M. Lukin, R. L. Walsworth, M. Loncar, and A. Yacoby, A robust scanning diamond sensor for nanoscale imaging with single nitrogen-vacancy centres, Nat. Nano **7**, 320 (2012).

[23] P. Tangyunyong, Thermal modeling of localized laser heating in multi-level interconnects, Microelectron. Reliab. **43**, 297 (2003).

[24] A. Orozco, J. Gaudestad, N. Gagliolo, C. Rowlett, E. Wong, A. Jeffers, B. Cheng, F. Wellstood, A. Cawthorne, and F. Infante, in *International Symposium for Testing and Failure Analysis* (2013), p. 189, https://dl.asminternational.org/istfa/proceedings-abstract/ISTFA2013/80224/189/11779.

[25] J. Gaudestad, N. Gagliolo, V. V. Talanov, R. H. Yeh, and C. J. Ma, in *Proceedings of the 20th IEEE International Symposium on the Physical and Failure Analysis of Integrated Circuits (IPFA)* (2013), p. 347, https://ieeexplore.ieee.org/document/6599179.

[26] F. S. Felt, in *International Symposium for Testing and Failure Analysis (ISTFA)* (2005), p. 169, https://dl.asminternational.org/istfa/proceedings-abstract/ISTFA2005/30880/169/9614.

[27] B. D. Schrag, M. J. Carter, X. Liu, J. S. Hoftun, and G. Xiao, in *Conference Proceedings from the 32nd International Symposium for Testing and Failure Analysis (ISTFA)* (2006), p. 13, https://dl.asminternational.org/istfa/proceedings-abstract/ISTFA2006/30897/13/11146.

[28] A. Pu, D. Thomson, and G. Bridges, Location of current carrying failure sites in integrated circuits by magnetic force microscopy at large probe-to-sample separation, Microelectron. Eng. **86**, 16 (2009).

[29] J. R. Kirtley and J. P. Wikswo, Scanning SQUID microscopy, Annu. Rev. Mater. Sci. **29**, 117 (1999).

[30] D. Broadway, S. Lillie, S. Scholten, D. Rohner, N. Dontschuk, P. Maletinsky, J.-P. Tetienne, and L. Hollenberg, Improved Current Density and Magnetization Reconstruction Through Vector Magnetic Field Measurements, Phys. Rev. Appl. **14**, 024076 (2020).

[31] A. Horsley, P. Appel, J. Wolters, J. Achard, A. Tallaire, P. Maletinsky, and P. Treutlein, Microwave Device Characterization Using a Widefield Diamond Microscope, Phys. Rev. Appl. **10**, 044039 (2018).

[32] O. Breitenstein, C. Schmidt, F. Altmann, and D. Karg, in *Microelectronics Failure Analysis Desk Reference* (ASM International, Materials Park, Ohio, USA, 2004), p. 330.